Supplementary Figures

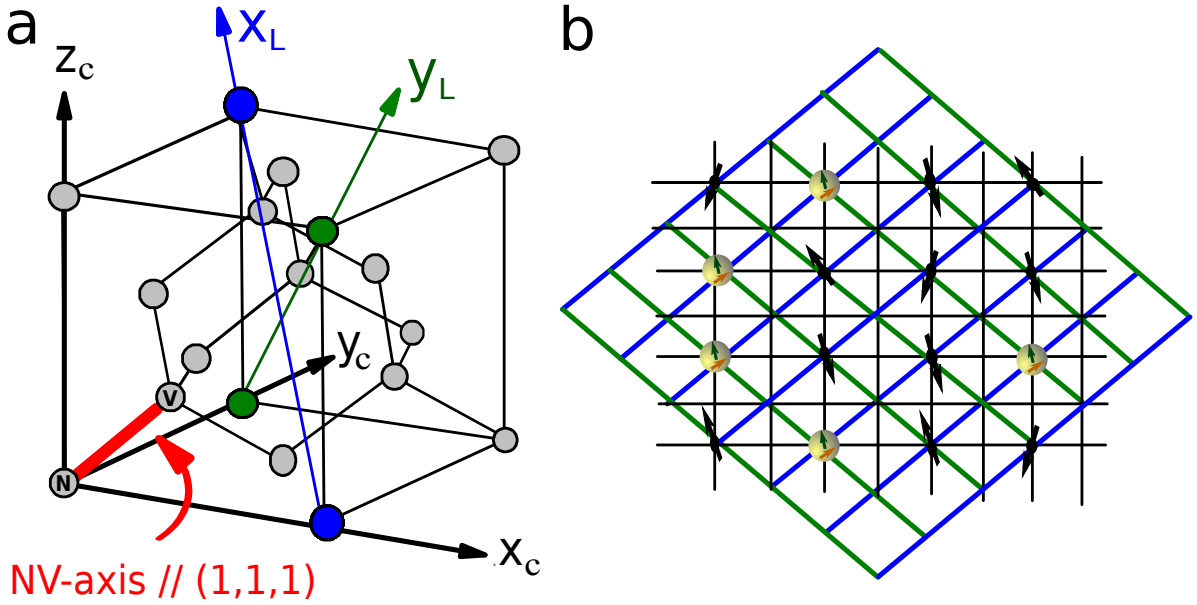

Supplementary Fig. S1: NV Schematic and Computational Plane (a) Depicts the diamond unit cell with corresponding NV axis $\parallel (1,1,1)$. The underlying lattice of the 2D array can be chosen with x_L and y_L defining the lattice grid (where (x_c, y_c, z_c) represent the Cartesian basis). For simplicity, in the derivations, we assume a $(1,1,1)$-cut diamond, whereby the plane of the cut is parallel to the computational plane spanned by x_L and y_L. (b) In this particular case, all NV centers and Nitrogen impurities sit in the computational plane defined by x_L, y_L. We note that this choice of axes is in slight contrast to the main text, where for simplicity $\hat{x}, \hat{y}$ is chosen to represent the lattice in which all spins lie. Dark spins represent Nitrogen impurities while NV centers are represented as pairs of green (electronic) and yellow (nuclear) spins (in analogy to the main text). Here, in contrast to the sparsely occupied plaquettes in the main text, we have chosen to occupy all potential sites in the computational plane with spins for illustrative purposes.

Supplementary Methods

Realization of Dark Spin Chain Data Bus with Nitrogen Impurities

We consider a dipole-dipole coupled chain of nitrogen impurities which forms the basis for the DSCB that couples remote NV registers. The Hamiltonian for a single Nitrogen impurity is given by

$$H_N = g_e\mu_B\vec{B}\cdot\vec{S} - g_N\mu_N\vec{B}\cdot\vec{I} + A_\parallel S_{z'}I_{z'} + A_\perp(S_{x'}I_{x'} + S_{y'}I_{y'}), \tag{S1}$$

where $A_\parallel = -159.7$MHz and $A_\perp = -113.8$MHz are the hyperfine constants corresponding to the primed axes, which is chosen with the Jahn-Teller (JT) axis as z'. As in recent reports, we consider the application of a magnetic field $\vec{B}$ of strength B_z (~ 1T), as defined in the main text, throughout the 2D array along the NV axis (consider e.g. $\hat{NV} \parallel (1,1,1)$), which defines the quantization axis $\hat{z}$. The existence of this large magnetic field implies that the ability to fabricate and control the crystallographic direction of the NV axis is of critical importance; indeed, recent work in this direction has demonstrated the possibility of aligning NV-axes during growth [60]. We envision the structural schematic of our architecture to enable optical access from above the bulk diamond sample, while coherent MW manipulations are achieved via microcoil arrays below the sample. To model the additional Jahn-Teller frequencies applied in the super-plaquettes, we calculate the impurity chain Hamiltonian between two nitrogens with differing Jahn-Teller axes (assuming a $(1,1,1)$ cut diamond, as shown in Supplementary Fig. S1), and with the JT axis of N_1 parallel to the NV axis (note that the non-parallel JT axes are equivalent to one another relative to the NV axis). We explicitly represent the hyperfine interaction within a standard Cartesian basis by choosing the Jahn-Teller axis of the first nitrogen N_1 as $e_{z'} \parallel (1,1,1)$ and subsequently $e_{x'} \parallel (2,-1,-1)$ and $e_{y'} \parallel (0,1,-1)$, and of the second nitrogen N_2 as $e_{z'} \parallel (1,1,-1)$ and subsequently $e_{x'} \parallel (-2,1,-1)$ and $e_{y'} \parallel (0,1,1)$ (the generalization to other pairs of JT axes follows after). Here, the hyperfine interaction of N_1 then takes the form $H_{HF} = A_\parallel S_zI_z + A_\perp(S_xI_x + S_yI_y)$, while the hyperfine term of the N_2 takes the form $\frac{1}{3}A_\parallel(\frac{S_z}{\sqrt{3}} + \frac{2S_x}{\sqrt{6}} + \frac{2S_y}{\sqrt{2}})(\frac{I_z}{\sqrt{3}} + \frac{2I_x}{\sqrt{6}} + \frac{2I_y}{\sqrt{2}}) + A_\perp[\frac{1}{6}(\frac{-2S_z}{\sqrt{3}} + \frac{2S_y}{\sqrt{2}} - \frac{4S_x}{\sqrt{6}})(\frac{-2I_z}{\sqrt{3}} + \frac{2I_y}{\sqrt{2}} - \frac{4I_x}{\sqrt{6}}) + \frac{1}{2}(\frac{2S_z}{\sqrt{3}} - \frac{2S_x}{\sqrt{6}})(\frac{2I_z}{\sqrt{3}} - \frac{2I_x}{\sqrt{6}})]$. It is important to note that the electronic Zeeman term in the impurity Hamiltonian provides a shift ~ 10GHz and that the nuclear Zeeman term provides a shift ~ 1MHz. Thus, to good approximation, we can disregard electronic spin flip terms proportional to S_x and S_y since the hyperfine constants are two orders of magnitude smaller than the electronic Zeeman energy, yielding $H_{HF} \approx A_\parallel S_zI_z$ for N_1 and

$$H_{HF} \approx S_zI_z(\frac{A_\parallel}{9} + \frac{8A_\perp}{9}) + S_z(\frac{A_\parallel}{3\sqrt{3}} - \frac{A_\perp}{3\sqrt{3}})(\frac{2I_x}{\sqrt{6}} + \frac{2I_y}{\sqrt{2}}) \equiv S_z(\gamma I_z + \alpha I_x + \beta I_y) \tag{S2}$$

for N_2, where $(\alpha,\beta,\gamma) = (-7.2,-12.5,-118.9)$MHz. For N_2, the hyperfine subspace is separated into two manifolds of nuclear spin $1/2$ and $-1/2$; to see that the nuclear spin-flip terms are highly off-resonant, it is easiest to work in a rotated basis with $\hat{\tilde{z}} = \frac{1}{\sqrt{\alpha^2+\beta^2+\gamma^2}}(\alpha\hat{x} + \beta\hat{y} + \gamma\hat{z})$, $\hat{\tilde{x}} = \frac{1}{\sqrt{\alpha^2+\gamma^2}}(-\gamma\hat{x} + \alpha\hat{z})$, and $\hat{\tilde{y}} = \frac{\beta\gamma}{\sqrt{(\alpha^2+\gamma^2)(\alpha^2+\beta^2+\gamma^2)}}(\frac{\alpha}{\gamma}\hat{x} - \frac{1}{\beta}(\gamma + \frac{\alpha^2}{\gamma})\hat{y} + \hat{z})$, wherein $H_{HF} \approx \sqrt{\alpha^2+\beta^2+\gamma^2}S_zI_{\tilde{z}}$. In the rotated basis, nuclear spin flips are captured by the Zeeman term $-g_N\mu_NB_0I_z = -g_N\mu_NB_0(\frac{\gamma}{\sqrt{\alpha^2+\beta^2+\gamma^2}}I_{\tilde{z}} + \frac{\alpha}{\sqrt{\alpha^2+\gamma^2}}I_{\tilde{x}} + \frac{\beta\gamma}{\sqrt{(\alpha^2+\gamma^2)(\alpha^2+\beta^2+\gamma^2)}}I_{\tilde{y}})$. Thus, for a given electronic spin, the nuclear spin subspaces are separated by $\sqrt{\alpha^2+\beta^2+\gamma^2} \sim 100$MHz, while the strength of the nuclear spin flip terms proportional to $I_{\tilde{x}}$ and $I_{\tilde{y}}$ ~ 100kHz and can hence be neglected. These secular approximations yield a nearest neighbor Hamiltonian given by (returning to the original basis for simplicity of notation)

$$H_{nn} = g_e\mu_BB_0(S_z^1 + S_z^2) - g_N\mu_NB_0(I_z^1 + I_z^2) + A_\parallel S_z^1I_z^1 + S_z^2I_z^2(\frac{A_\parallel}{9} + \frac{8A_\perp}{9}) + \frac{\mu_0}{4\pi r^3}g_e^2\mu_B^2(S_z^1S_z^2), \tag{S3}$$

where we have additionally neglected electronic spin flip terms originating from dipole-dipole interactions between the impurities since their hyperfine terms vary by ~ 10MHz while the dipole coupling strength is only ~ 10kHz for 20nm separation (neglecting the field gradient). Thus, in the case where neighboring impurities have differing Jahn-Teller axes, the electronic spin flip terms can always be neglected to give an Ising interaction. In the case of parallel Jahn-Teller axes, when the neighboring nitrogen nuclear spins are different, the combined hyperfine term takes the form $\pm(S_z^1 - S_z^2)(\frac{A_\parallel}{6} + \frac{A_\perp}{3})$. The dipole-dipole terms which correspond to electronic spin flipping will attempt to couple $|\uparrow_1,\downarrow_2\rangle$ and $|\downarrow_1,\uparrow_2\rangle$; however, this coupling is again highly suppressed since these states are separated by $(\frac{A_\parallel}{3} + \frac{2A_\perp}{3}) \sim 100$MHz, while the dipole coupling strength is ~ 10kHz. Furthermore, the states $|\uparrow_1,\uparrow_2\rangle$ and $|\downarrow_1,\downarrow_2\rangle$ are separated from the others by the electronic Zeeman energy, ensuring that dipole-dipole induced spin flips will again be highly off-resonant. Finally, when the Jahn-Teller axes are parallel and the nuclear spins are also identical, these dipolar spin-flip terms are suppressed by the external magnetic field gradient. It is important to

note that for each Nitrogen spin, since the hyperfine term can take on four possible values, all four frequencies, corresponding to $\omega_0 \pm \frac{1}{2}A_\parallel$ and $\omega_0 \pm \frac{1}{2}(\frac{A_\parallel}{9} + \frac{8A_\perp}{9})$ are applied in order to address the impurity (ω_0 as defined in equation (2) of the main text).

In addition to the properties associated with single Nitrogen impurities, we now consider the NV-N interaction and show that it is possible to distill an Ising interaction. The NV Hamiltonian is given by

$$H_{NV} = g_e\mu_B B_z S_z - g_N\mu_N B_z I_z + A_{NV}(S_z I_z + S_x I_x + S_y I_y) + \Delta_0 S_z^2 \tag{S4}$$

where $A_{NV} = 3.1$MHz and $\Delta_0 = 2.87$GHz is the zero-field splitting of the singlet. For the purposes of this derivation, we will consider the $m_s = 0, 1$ states to be the NV electronic qubit and will disregard the $m_s = -1$ state which is far-detuned (Zeeman shifted away due to the ~ 1T magnetic field). The flip terms between the electronic and nuclear spin ($S^+I^- + S^-I^+$) of the NV are suppressed due to the zero-field splitting and the large magnetic field, since $\Delta_0, g_e\mu_B B_z \gg A_{NV}$. The dipole-dipole interactions between the NV electronic spin and an impurity electronic spin will be nearly identical to the impurity-impurity dipole coupling which has previously been considered. In particular, considering quantization along the NV axis, which for simplicity will also be the assumed Jahn-Teller axis (the result is analogous for other JT orientations), and noting that the unit vector pointing from the NV to the N-impurity lies in the computational plane defined by the normal vector $(1, 1, 1)$, we find that the Hamiltonian is (under the secular approximation in analogy to Sec. IA),

$$H = g_e\mu_B B_z(S_z^{NV} + S_z^N) - g_N\mu_N B_z(I_z^{NV} + I_z^N) + A_{NV}S_z^{NV}I_z^{NV} + \Delta_0(S_z^{NV})^2 + A_\parallel S_z^N I_z^N + \frac{\mu_0}{4\pi r^3}g^2\mu_B^2 S_z^{NV}S_z^N \tag{S5}$$

To keep only the Ising interaction term, we require ω_{NV}, ω_N, and $|\omega_{NV} - \omega_N|$ to all be much greater than the strength of the dipole coupling, where ω_{NV} is the coefficient of S_z^{NV} and ω_N is the coefficient of S_z^N.

Control of Directionality in Free Fermion State Transfer

We consider the Hamiltonian presented in equation (4) in the main text. Under the assumption that $g \ll \frac{\kappa}{\sqrt{N}}$, we work perturbatively in eigenstates of the bare Hamiltonian $H_0 = \sum_{i=1}^{N-1}\kappa(S_i^+S_{i+1}^- + S_i^-S_{i+1}^+)$, and consider coupling through the perturbation Hamiltonian $H' = g(S_{NV_1}^+S_1^- + S_{NV_2}^+S_N^- + \text{ h.c. })$. The essence of FFST can be understood as the long-range coherent interaction between the spin qubits, mediated by a specific collective eigenmode of the intermediate spin chain. This mode is best understood via Jordan-Wigner (JW) fermionization [61–63], which allows for the states of an XX spin chain to be mapped into the states of a set of non-interacting spinless fermions. In this representation, the state transfer is achieved by free fermion tunneling. By ensuring that the end spin qubits are weakly coupled to the intermediate spin chain, it is possible to tune the NV registers to achieve resonant tunneling through only a single particular fermionic eigenmode. Particle-hole symmetry of the Hamiltonian implies that the energy spectrum of the single fermion manifold is mirror symmetric across $E = 0$. This implies that in the case of even N intermediate spin chains (which are uniquely present in the proposed architecture), the NV registers are always initially off-resonant from all fermionic eigenmodes of both left and right spin chains.

In this context, directionality becomes easily achievable so long as the left and right spin chains are of differing lengths, since the single fermion spectrum will then be different. Thus, by ensuring that g is sufficiently small, it is possible to tune to and hence be resonant with only a single spin chain direction. In particular, the energy spectrum of the single fermion manifold is given by $E_k = 2\kappa\cos\frac{k\pi}{N+1}$, where $k = 1, \cdots, N$; thus, tuning to a particular fermionic eigenmode corresponds to making choices of Δ and Ω which ensure that $\Delta - \Omega_N \approx E_k$. The specific choice of k corresponds to the particular single fermion eigenmode which is being tuned to. Interestingly, this can allow for control over the speed of quantum state transfer. This speed is maximimized for $k = \frac{N}{2} \pm 1$ in the case of even N chains and for $k = \frac{N+1}{2}$ in odd N chains. Directional control over state transfer is achieved by ensuring that only either the left or right DSCB is resonant with the NV register. In this scenario, the coupling between the NV and the neighboring spin chain, which is off-resonant is highly suppressed. Assuming that the two neighboring spin chains are of differing lengths N_1 and N_2, the characteristic energy separation between fermionic eigenmodes in the two chains is approximately $\frac{\kappa}{N_1} - \frac{\kappa}{N_2} = \frac{\kappa(N_1-N_2)}{N_1N_2}$. Thus, by ensuring that the register-impurity coupling g is smaller than such an energy separation, it is possible to ensure that only single directional FFST occurs. Additionally, such an analysis suggests that by tuning g, it may be possible to overcome coupling-strength disorder induced by imperfect impurity implantation. In particular disorder will cause localization, asymmetry of the eigenmodes, and changes in the statistics of the eigenenergies. In the case of coupling-strength disorder, there exists an extended critical state at $E = 0$ with a diverging localization length; this ensures the existence of an extended eigenmode with a known eigenenergy, suggesting that FFST is intrinsically robust against coupling-strength disorder. However, the existence of an extended mode is not sufficient to ensure state transfer as disorder also enhances off-resonant tunneling rates and causes the eigenmode wavefunction amplitude to become asymmetric at the two ends of the chain. Despite such imperfections, by individually tuning the qubit-chain couplings, g_{left} and g_{right}, it is possible to compensate for eigenmode asymmetry; furthermore, sufficiently decreasing the magnitude of the qubit-chain coupling ensures that off-resonant tunneling can safely be neglected, even in the presence of disorder.

As mentioned in the main text, it is essential to consider the intrinsic properties of the dark Nitrogen impurity spin chain; in particular, the room temperature $T_1^N \approx 2$ms time of the Nitrogen impurity is limited by dynamic Jahn-Teller reorientation [64, 65]. Thus, nominally, the total time required for both DSCB mediated coherent coupling protocols introduces a significant depolarization error if we consider limitation by the impurity T_1^N time. However, at room temperature, the dynamic Jahn-Teller (JT) reorientation is governed by tunneling between the four tetrahedrally symmetric axes, and the associated rate is given by

$$1/T_1^N = 4 * 10^{12} e^{-\epsilon/kT} \mathrm{s}^{-1}, \tag{S6}$$

where $\epsilon = 0.76$eV is the experimentally determined activation energy. This exponential dependence on both activation energy and temperature suggests that a combination of a static electric field ($\sim 10^6$V/cm) [66–68] and slight cooling ($T \approx 250$K) can extend T_1^N to above 10s. Hence, in the discussion of operational errors in the main text, we have assumed limitation by T_1^{NV}, the spin-lattice relaxation time of the NV center.

Simulations and Error Optimization

We consider the optimization of errors in the context of the DSCB mediated remote register coupling. First, we consider the accumulated infidelity associated with the adiabatic SWAP sequence, represented by equation (5) in the main text, $p_{err}^{SS} \approx N(p_{adia} + p_{off}^{SS} + p_{dip} + p_{T1}^{SS} + p_{T2}^{SS})$. Re-expressing p_{err}^{SS} to capture the form of the associated infidelity yields

$$p_{err}^{SS} \approx N \left[\frac{1}{(\kappa' t_{ss})^2} + \frac{\Omega_i^2}{\Delta_g^2} + \left(\frac{\kappa'}{\Omega_i}\right)^2 + \frac{t_{ss}}{T_1^{NV}} + \left(\frac{t_{ss}}{T_2^{NV}}\right)^3 + \left(\frac{t_{ss}}{T_2^{N}}\right)^3 \right], \tag{S7}$$

where t_{ss} represents the time required to SWAP between a single pair of impurities, κ' represents an optimized coupling strength, Ω_i represents the Rabi frequency on the impurities, $\Delta_g \sim 10$MHz represents the gradient-induced splitting for a magnetic field gradient $\sim 10^5$T/m, $T_1^{NV} \approx 350$ms, and we assume all dephasing rates are limited by $T_2^{NV} \approx 5-10$ms (see Sec. IIC for details on Δ_g derivation). The assumption of T_2^{NV} limited dephasing rates is consistent with recent measurements of $T_2^N \sim 0.25$ms, which were performed in natural ^{13}C abundance diamond samples [69]; hence, in direct analogy to T_2^{NV}, it is expected that isotopic purification may well enhance such coherence times by more than an order of magnitude. Here, we describe the error terms in more detail to evince the origin of the infidelity. The first term in p_{err}^{SS} corresponds to the non-adiabatic correction resulting from an optimized adiabatic ramp profile. The second term represents off-resonant excitations induced by Ω_i. The third term corresponds to additional off-resonant errors induced by the finite initial splitting as well as by dipole-dipole coupling of next-to-nearest neighbor impurities; since the dipolar interaction strength $\sim \kappa'$ while the characteristic energy spacing between impurities $\sim \Omega_i$, the associated error is $\left(\frac{\kappa'}{\Omega_i}\right)^2$. The fourth error term corresponds to the depolarization error induced by the finite NV T_1 time, t_{ss}/T_1^{NV}. The final two error terms correspond to the infidelity induced by dephasing of the NV center and the P1 center respectively, $1 - e^{-\left(t_{ss}/T_2^{NV}\right)^3} \approx (\frac{t_{ss}}{T_2^{NV}})^3$ and $1 - e^{-\left(t_{ss}/T_2^{N}\right)^3} \approx (\frac{t_{ss}}{T_2^{N}})^3$.

The combined total error can be numerically optimized with respect to t_{ss} and Ω_i. A crucial point to note here is the importance of the coherence time of the substitutional P1 centers (Nitrogen impurities) forming the dark spin chain; this is particularly relevant in the case of the adiabatic sequential SWAP since the quantum information is localized on the various P1 centers during the majority of the state transfer. Furthermore, we note that the current form of p_{T2} assumes that only a single echo pulse is applied during an individual SWAP. This suggests that the functional form of the infidelity can be significantly improved by increasing the number of echo pulses, with the extended coherence time scaling as $\sim N_p^{2/3}$ where N_p is the number of pulses ($N_p > 100$ has already been experimentally demonstrated) [70, 71]; in fact, we expect that such an effect can easily be achieved in our system due to the assumed strong driving [70, 71]. Numerically optimizing the full infidelity p_{err}^{SS} in parameters t_{ss} and Ω_i (for $N = 18$), yields $\Omega_i \approx 800$kHz and $Nt_{ss} \approx 5$ms with total error $\approx 4 \times 10^{-2}$, consistent with the full numerical simulations presented in the main text. While the current optimization utilizes the bare coherence times, by taking into account dynamic decoupling, it is possible to demonstrate that to good approximation, dephasing errors can be neglected since they will not participate in the dominant balance of the optimization. In particular, we find that $p_{T2}^{SS} \approx N[t_{ss}/(T_2^N N_p^{2/3})]^3 < 10^{-3}$ when only a small number of pulses, $N_p \approx 10$ is applied. Hence, in the remaining error analysis, we assume that dephasing-induced errors can be safely neglected. We note that the full numerical simulations presented in the main text account for the additional Jahn-Teller (MW) frequencies utilizing a Floquet formalism and are obtained through numerical integration of the Schrödinger equation with the optimized adiabatic SWAP profile [72]. Non-unitary errors corresponding to depolarization are then added to the unitary errors and the total infidelity is subsequently optimized [73].

Before considering the numerical optimization of the infidelity associated with FFST, we address the issue of disordered coupling strengths in the adiabatic sequential SWAP. In particular, implantation errors associated with the dark spin chain imply that nearest neighbor coupling strengths between the various Nitrogen impurities will not be precisely known; this imprecision will

cause the qubits to accumulate an unknown phase during each adiabatic SWAP operation. One possible solution is to characterize the energy spectrum and coupling strengths of the intermediate spin chain; in particular, despite the fact that quantum control and optical access are restricted to the NV registers, it is possible to indirectly characterize all couplings of the intermediate chain through tomography on only a single register located at the end of the spin chain [74]. Once these couplings are known, it may be possible to correct for unitary errors at each step along the adiabatic SWAP since the dark P1 centers are individually addressable (via the field gradient).

A simpler alternative to overcoming the above unitary errors is to implement a spin-echo type global π-pulse following the first set of sequential SWAP gates. Indeed, after the quantum information has been sequentially swapped from one end of the chain to the other, an entangling CP-gate between the nuclear memory and the swapped qubit is performed. Then, we implement a global π-pulse on all Nitrogen impurity spins along the chain as well as the end qubits; this ensures that the second (reverse) set of sequential SWAP gates designed to return the qubit to the original register will cancel the unknown phase accumulated during the first set of SWAPs. This can be seen as follows: During the adiabatic SWAP of a pair of qubits, an initial state of the form $|\phi\rangle = c_1|00\rangle + c_2|01\rangle + c_3|10\rangle + c_4|11\rangle$ becomes $|\phi'\rangle = c_1|00\rangle + c_2e^{i\theta}|10\rangle + c_3e^{-i\theta}|01\rangle + c_4|11\rangle$, where θ characterizes the unknown acquired phase. By flipping all spins through a global π-pulse, the state becomes $|\phi'\rangle = c_1|11\rangle + c_2e^{i\theta}|01\rangle + c_3e^{-i\theta}|10\rangle + c_4|00\rangle$, which upon a reverse step of adiabatic SWAP yields $|\phi''\rangle = c_1|11\rangle + c_2|10\rangle + c_3|01\rangle + c_4|00\rangle$. Finally, another global π-pulse is implemented, to yield $|\phi''\rangle = c_1|00\rangle + c_2|01\rangle + c_3|10\rangle + c_4|11\rangle$. This implies that the proposed alternative protocol will ensure that the unknown phases accumulated during the two segments of state transfer effectively cancel one another, ultimately leaving only the desired long-range CP-gate.

Now, we consider the accumulated infidelity associated with FFST, represented by equation (6) in the main text $p_{err}^{FFST} \approx p_{off}^{FFST} + p_f + p_g + p_{T1}^{FFST}$ (neglecting p_{T2}^{FFST} as discussed above). Re-expressing p_{err}^{FFST} to capture the form of the associated infidelity yields

$$p_{err}^{FFST} \approx \frac{\Omega_N^2 + \Omega^2}{(\Delta_g)^2} + (\frac{g/\sqrt{N}}{\kappa/N})^2 + (\frac{\kappa}{\Delta})^2 + N\frac{t_{FFST}}{T_1^{NV}}, \tag{S8}$$

where Ω_N corresponds to the Rabi frequency applied on the impurity, Ω corresponds to the Rabi frequency applied on the NV register, $\kappa \approx 12.6$kHz, t_{FFST} represents the total time required for state transfer, and Δ corresponds to the NV detuning as defined in the Methods section in the main text. Here, we describe the error terms in more detail to evince the origin of the infidelity. The first term in p_{err}^{FFST} corresponds to the off-resonant excitation of an NV register. Similarly, the second term also results from an off-resonant error and corresponds to undesired coupling with off-resonant fermionic modes. Since the coupling strength is characterized by $g/\sqrt{N}$, while the characteristic eigenenergy splitting $\sim \kappa/N$, such an off-resonant error induces an infidelity $(\frac{g/\sqrt{N}}{\kappa/N})^2$. The third error term results from the protocol designed to achieve controlled coupling g, as elucidated in the Methods. Finally, directly analogous to p_{err}^{SS}, the final term corresponds to the error induced by the operational time, $t_{FFST} \sim \sqrt{N}/g$, which results in depolarization. However, it is essential to note that relative to the adiabatic sequential SWAP, there is an additional factor of N in p_{T1}^{FFST}.

This factor results from the generation of multi-partite entanglement via a set of controlled-phase gates during a single FFST step; despite such entanglement, remote register coupling is readily achieved because a second transfer step (corresponding to the return of the quantum information to the original NV as shown in Fig. 3C of the main text) disentangles the quantum information from the intermediate dark spin chain data bus. Crucially, the local two-qubit gate which is performed in the middle of two FFST steps must commute with the controlled-phase multi-partite entanglement. In particular, the two-qubit operation depicted in Fig. 3C could be a local CP-gate, which would be preserved in the disentangling step. Combined with single qubit rotations, a controlled-phase gate allows for arbitrary two-qubit gates and hence universal computation.

The controlled coupling g is achieved by utilizing the NV three-level structure, whereby $g \sim \kappa\frac{\Omega}{\Delta}$ (as discussed in Methods section of the main text), allowing for the re-expression of g in p_{err}^{FFST}. Similarly, since FFST requires tuning to a particular fermionic eigenmode, it is also possible to re-express $\Delta \approx \Omega_N$ (see Sec. IIB for details on fermion tuning). These re-expressions allow for numerical optimization in the two parameters Ω_N and Ω yielding $\Omega_N \sim 285$kHz and $\Omega \sim 95$kHz, with total operational errors $\approx 2.4 \times 10^{-2}$ and total transfer time $t_{FFST} = 0.21$ms (where we have utilized parameters: $T_1^{NV} = 250$ms and $N = 7$), in good agreement with the full numerical simulations presented in the main text. The numerical simulations of FFST also account for the additional Jahn-Teller frequencies and are obtained through full Hamiltonian diagonalization. Non-unitary errors corresponding to depolarization are then added and the total infidelity is subsequently optimized [73].

The optimizations presented above rely on the ability to control the spatial separation of impurity arrays during implantation patterning. Recent advances have enabled sub-100nm resolution diamond spin-patterning [75, 76] and further enhanced resolution $<$ 30nm is also possible [77]. As discussed in the maintext, in the case of FFST, although disordered implantation may cause eigenenergies to shift, by tuning the NV registers, one can overcome such errors. Furthermore, in the case of the adiabatic SWAP, even when coupling strengths are varied, perfect adiabatic SWAP can be achieved as long as the rate at which Ω_i and Ω_{i+1} are ramped through one another is sufficiently small. Moreover, both DSCB methods can be rendered completely

robust against implantation errors if one can tomographically characterize the intermediate chain [74]. In the case of FFST, such tomography will enable the direct identification of eigenmodes. In the case of the adiabatic sequential SWAP, tomography will enable perfect timing of each individual gate, since pairwise coupling strengths will be known.

Full Frequency Spectrum in Super-plaquettes

As mentioned in the main text during consideration of operational errors, the frequency spectrum of a given super-plaquette requires careful consideration. Indeed, it is crucial to ensure that off-resonant cross-talk can be suppressed through optimization of the field gradient. In particular, given a sufficiently large magnetic field gradient, it will be essential to consider the full range of frequencies covered throughout a super-plaquette. For example, although the NV zero-field splitting (ZFS) $\Delta_0 \sim 3$GHz naively protects the register from off-resonant excitations during impurity manipulation, it is important to note that this static ZFS is bridged as rows progress vertically along the field gradient. Given a gradient of order $100\text{MHz}/10\text{nm}$ (in this section, for simplicity, we assume 10nm row separation), a displacement of only 30 rows along the gradient direction is sufficient to fully bridge the NV ZFS. Furthermore, since each Nitrogen impurity requires four separate frequencies to be addressed, it is essential to ensure that such a congested frequency spectrum within a super-plaquette does not render the error probability intolerable. As discussed, the four frequencies corresponding to each Nitrogen impurity result from the two possible nuclear spin states and the choice of whether the JT axis lies along the NV axis; hence, the possible frequencies are $\omega_0 \pm 1/2A_{\parallel} = \omega_0 \pm 80$MHz and $\omega_0 \pm 1/2(\frac{A_{\parallel}}{9} + \frac{8A_{\perp}}{9}) = \omega_0 \pm 60$MHz. To describe an adequate framework regarding the frequency spectrum, it is possible to consider a simplified problem, in which we ignore the nuclear spin and thus, are left with three transitions corresponding to the two NV transitions ($|0\rangle \rightarrow |\pm 1\rangle$) and the Nitrogen impurity transition. For a static magnetic field that gives a Nitrogen ESR frequency equal to ω_0, the NV transitions correspond to $\omega_0 + 3$GHz and $\omega_0 - 3$GHz. Thus, we can describe the situation according to three base lines at $-3, 0, 3$GHz, where the full frequency spectrum within the super-plaquette results from the addition of all possible lines at subsequent 10nm intervals.

One possible solution to avoid frequency overlap is to choose the field gradient to be $3 * \zeta\text{MHz}/10\text{nm}$, where ζ is as yet undetermined. The possible choices of ζ correspond to field gradients which for some $n \in \mathbb{Z}$ yield that after $n * 10$nm, the field due to the gradient is $3\text{GHz} - \zeta$. Such a choice immediately ensures that (disregarding JT) all possible transitions within a super-plaquette are non-overlapping. Furthermore, by correctly choosing ζ, it is possible to ensure that even within the context of addressing the four individual Nitrogen impurity transitions, the separation of any pair of nearest frequencies is ~ 10MHz. A simple example can be illustrated by considering a gradient with strength $150\text{MHz}/10\text{nm}$, where the absolute minimum spacing between any two frequencies in a super-plaquette is $\Delta_g = 10$MHz.

Supplementary Notes

Note 1: Using Laguerre-Gaussian Donut Beams

In the maintext, we mentioned two possible approaches to using Laguerre-Gaussian (LG) donut beams to further enhance our scalable architecture. First, we discussed the possibility of using a *red* LG donut to enhance the readout fidelity. Second, we discussed the possibility of using a *green* LG donut to enable subwavelength coherent control. Here, we provide a detailed discussion of the associated errors and error suppression in both cases.

A *red* LG beam, which is detuned from the optical transition will only induce stimulated decay of an NV center, but will never induce optical cycling. In this way, those illuminated NVs situated in the red LG circumference will be dominated by stimulated emission, leaving only the desired readout NV (in the donut center) to emit spontaneously for fluorescent detection. Moreover, such a red LG donut will also help suppress the undesired decoherence of neighboring NV registers. Indeed, it is favorable to induce the fast stimulated decay of such neighboring centers since this will suppress the NV-excited state lifetime, thereby limiting the effective dephasing of the nuclear spin memory. In particular, we can estimate the decoherence of the nuclear spin qubit of a neighboring register during optical readout. With a highly focused green Gaussian laser beam, the probability to excite a neighboring NV center can be very small. In particular, for a beam waist of 200nm, the optical intensity at 500nm (e.g. the separation between plaquettes) is only 3×10^{-6} of the beam center. Thus, the error probability associated with an unintended excitation is roughly $p_1 \sim 3 \times 10^{-6}$ for each readout attempt. Next, the stimulated emission induced by the red LG beam can reduce the excited state lifetime from 10ns to $\tau' = 0.1$ns (or less). Assuming that the excited state has a large hyperfine coupling $A' = 40(2\pi)$MHz, yields an effective error probability, $p_2 = (A'\tau')^2 = 0.03$ for each unintended optical excitation. In combination, the overall error probability associated with each attempted readout is $p_1 p_2 \sim 10^{-7}$. Even after thousands of readout repetitions, the error probability of neighboring NVs can be controlled to below 0.1% and hence can be safely neglected in our discussion. Thus, our above error analysis demonstrates that the use of a red LG beam for stimulated emission can indeed provide a further enhancement in our readout fidelity.

Furthermore, the use of *green* Laguerre-Gaussian optical donut beams may enable the subwavelength selective manipulation of individual NV registers. Here, we consider the dominant imperfection in such subwavelength control: The residual optical excitation rate κ_0 for an unilluminated NV register in the dark donut center (due to imperfect destructive interference). We estimate that the error probability for the selected (e.g. resonant and unilluminated) NV register is: $p_{err,\text{selected}} \approx \frac{\kappa_0}{\Omega_i}$, which characterizes the undesired optical excitation probability during time $1/\Omega_i$. Such an error must be optimized in the context of off-resonant cross-talk; however, given good interference contrast $\kappa_0/\kappa = 10^{-6}$, $p_{err,\text{selected}}$ can easily be rendered sub-percent. The notion of subwavelength register control also naturally suggests the importance of microcoil engineering as a necessary ingredient for our architecture; indeed, there has been tremendous recent progress demonstrating the possible optimization of planar microcoil arrays [78].

Note 2: NV Implantation and Conversion

Although we have considered various errors accumulated during single- and two-qubit gate operations, an important further consideration is the error associated with the imperfect positioning of Nitrogen ion implantations. This imperfect implantation leads to errors in both the coupling strength as well as the individual impurity ESR frequencies. Crucially, both the vertical adiabatic sequential SWAP and the horizontal FFST are robust to fluctuations in coupling strength. The adiabatic sequential SWAP is also robust to errors induced by ESR frequency variations. Such variations result in an effective Rabi frequency, which alters the start and end point of the optimized ramp profile, without significantly affecting the adiabatic passage. On the other hand, such ESR frequency fluctuations induce an off-resonant error during FFST; however, improvements in the implantation precision and utilizing larger Ω_N can sufficiently suppress such errors.

In addition to implantation errors, it is also important to consider the infidelity induced by imperfect NV conversion efficiency. In particular, current experiments are limited by an optimistic NV conversion efficiency of approximately 40%. Within the context of the current architecture design (Fig. 5), each plaquette contains 8 possible implantation sites that will allow for a staggered super-plaquette NV register structure, yielding a nominal error $\approx 10^{-2}$. Thus, each super-plaquette will have a filling fraction $\sim 99\%$ of functional plaquettes and the gate overhead associated with such faulty qubits will be negligible. Since the threshold penalty for faulty qubits is expected to be proportional to the gate overhead, the error threshold ϵ is expected to remain $\approx 1.4\%$ [79]. While plaquettes which do not contain an NV center will certainly contribute to errors, certain plaquettes will also contain multiple NV centers. Such errors will ideally be minimized by our proposed two-step implantation process, since individual Nitrogen impurities are implanted and annealed in each plaquette until the formation of an NV register. However, in the event that this occurs, we envision two possible solutions: first, the second implantation step corresponding to the fabrication of the DSCB can be tailored around the additional register so as to avoid its inclusion and second, the additional NV centers

can merely be considered elements of the DSCB. The electronic spin of these non-register NVs provide a natural alternative to the P1 electronic spin; furthermore, no quantum information will be stored in the nuclear spin of these non-register color centers ensuring that individual plaquettes can still be read out. However, since the control fields governing the quantum register will also affect these additional NV centers, the spin chain will contain weakened couplings at these locations; tomographical characterization of the spin chain eigenmodes will nevertheless enable FFST. Additionally, an intriguing possibility is to utilize the dark Nitrogen impurities as computational resources in and of themselves. In addition to an electronic spin, each P1 center also contains its own nuclear spin, which may be able to store quantum information; however, since each Nitrogen impurity is dark, readout would still need to occur via the NV center.

Finally, the zig-zag structure of the vertical impurity spin chain allows for connectivity between any NV lattice site and the lattice site directly above in the corresponding vertically adjacent plaquette, *as well as* any of the four nearest neighbor lattice sites in either direction (in order to account for imperfect conversion efficiency), as can be seen in Fig. 5. The implantation region of vertically adjacent plaquettes is somewhat limited by the particular location of NV registers in the preceding vertical plaquette; however, such errors can be made negligible by considering larger plaquette sizes and hence, a larger range of connected vertical sites through the impurity spin chain.

Supplementary References

[60] Edmonds, A. M. *et al.* Production of oriented nitrogen-vacancy color centers in synthetic diamond. Preprint at *arXiv:1112.5757v1* (2011).

[61] Jordan, P. and Wigner, E. Über das Paulische Äquivalenzverbot *Z Physik* **47**, 631 (1928).

[62] Bethe, H. On the theory of metals. 1. Eigenvalues and eigenfunctions for the linear atomic chain *Z Physik* **71**, 205 (1931).

[63] Lieb, E., Schultz, T. & Mattis, D. 2 Soluble models of an antiferromagnetic chain *Annals of Physics* **16**, 407 (1961).

[64] Zaritskii, I. M., Bratus, V. Y., Vikhnin, V. S., Vishnevskii, A. S., Konchits, A. A. & Ustintsev, V. M. Spin-lattice relaxation of Nitrogen Jahn-Teller center in diamond. *Fizika Tverdogo Tela* **18**, 11 (1976).

[65] Terblanche, C. J. & Reynhardt, E. C. Room-temperature field dependence of the electron spin-lattice relaxation times of paramagnetic P1 and P2 centers in diamond. *Chem. Phys. Lett.* **322**, 273-279 (2000).

[66] Averkiev, N. S., Gutkin, A. A., Il'inskii, S. Y. Electric-field and interface effects on the orientation of Jahn-Teller vacancy distortions in semiconductors. *Physics of the Solid State* **40**, 12 (1998).

[67] Trew, R. J. *et al.* The potential of Diamond and SiC electronic devices for microwave and millimeter-wave power applications *Proceedings of the IEEE* **79**, 5 (1991).

[68] Liu, P., Yen, R. & Bloembergen, N. Dielectric breakdown threshold, two-photon absorption, and other optical damage mechanisms in diamond *IEEE J. Quantum Electron* **QE14**, 574-576 (1978).

[69] Morton, J. J. L. & Tyryshkin, A. M. *private communication* (2011).

[70] de Lange, G. *et al.* Universal Dynamical Decoupling of a Single Solid-State Spin from a Spin Bath *Science* **330**, 60-63 (2010).

[71] Taylor, J. & Lukin, M. D. Dephasing of Quantum Bits by a Quasi-Static Mesoscopic Environment *Quantum Information Processing* **V5**, 503-536 (2006).

[72] Drese, K. & Holthaus, M. Floquet theory for short laser pulses. *Eur. Phys. J. D* **5**, 119-134 (1999).

[73] Nielsen, M. A. A simple formula for the average gate fidelity of a quantum dynamical operation *Physics Letters A* **303**, 249-252 (2002).

[74] Burgarth, D., Maruyama, K., & Nori, F. Coupling strength estimation for spin chains despite restricted access *Phys. Rev. A* **79**, 020305(R) (2009).

[75] Spinicelli, P. *et al.* Engineered arrays of nitrogen-vacancy color centers in diamond based on implantation of CN^- molecules through nanoapertures *New Journal of Physics* **13**, 025014 (2011).

[76] Toyli, D. M., Weis, C. D., Fuchs, G. D., Schenkel, T., & Awschalom, D. D. Chip-Scale Nanofabrication of Single Spins and Spin Arrays in Diamond *Nano Lett.* **10**, 3168-3172 (2010).

[77] Vieu, C. *et al.* Electron beam lithography: resolution limits and applications *Applied Surface Science* **164**, 111-117 (2000).

[78] Boero, G. *et al.* Electron-spin resonance probe based on a 100 μm planar microcoil. *Rev. Sci. Instrum.* **74**, 4794-4798 (2003).

[79] Fowler, A. G., Wang, D. S. & Hollenberg, L. C. L. Surface codes on faulty 2-D nearest neighbor lattices *Quant. Info. Comput.***11**, 8 (2011).